

Optimal Transition Paths for AMOC Collapse and Recovery in a Stochastic Box Model

JELLE SOONS,^a TOBIAS GRAFKE,^b AND HENK A. DIJKSTRA^a

^a*Institute for Marine and Atmospheric Research, Utrecht University, Princetonplein 5, 3584 CC Utrecht, The Netherlands*

^b*Mathematics Institute, University of Warwick, Coventry CV4 7AL, United Kingdom*

ABSTRACT: There is strong evidence that the present-day Atlantic Meridional Overturning Circulation (AMOC) is in a bi-stable regime and hence it is important to determine probabilities and pathways for noise-induced transitions between its equilibrium states. Here, using Large Deviation Theory (LDT), the most probable transition pathways for the noise-induced collapse and recovery of the AMOC are computed in a stochastic box model of the World Ocean. This allows us to determine the physical mechanisms of noise-induced AMOC transitions. We show that the most likely path of an AMOC collapse starts paradoxically with a strengthening of the AMOC followed by an immediate drop within a couple of years due to a short but relatively strong freshwater pulse. The recovery on the other hand is a slow process, where the North Atlantic needs to be gradually salinified over a course of 20 years. The proposed method provides several benefits, including an estimate of probability ratios of collapse between various freshwater noise scenarios, showing that the AMOC is most vulnerable to freshwater forcing into the Atlantic thermocline region. Moreover, a comparison with a quasi-equilibrium approach reveals the contrasts in behavior of a bifurcation-induced and a noise-induced collapse of the AMOC.

1. Introduction

The Atlantic Meridional Overturning Circulation (AMOC) is of paramount importance to Earth's climate (Srokosz et al. 2023). It consists of a northward transport of warm upper ocean water and a deeper southward flow of cool water. This northward heat transport is a major reason for the relatively mild climate in Western Europe. An important process behind this circulation is thought to be the water mass transformation in the subpolar North Atlantic Ocean. Here, the relatively warm and salty sea water transported from low latitudes is cooled by the atmosphere, and becomes the cold and salty North Atlantic Deep Water (NADW), which sinks and returns southward (Frajka-Williams et al. 2019).

Stommel (1961) realized that the AMOC is affected by two competing feedback effects due to the coupling of the circulation with the density field. When the AMOC strengthens, more heat will be transported northwards which will reduce deep water formation, providing a negative feedback via this thermal circulation. On the other hand, this strengthening also increases northward salt transport which increases deep water formation and hence is a positive feedback, the salt-advection feedback (Marotzke 2000). These feedbacks, and that the atmosphere damps ocean temperature anomalies much more strongly than salinity anomalies, create a multiple equilibrium regime for the AMOC. In the box model used in Stommel (1961), two stable equilibria exist under the same buoyancy forcing conditions. Such multiple equilibrium regimes have been found in a number of other box models of the AMOC (Rooth 1982; Rahmstorf 1996; Lucarini and Stone 2005; Cimadoribus et al. 2014) for which

the steady states can be computed when parameters are changed.

In more detailed models, the common procedure to investigate a possible multiple equilibrium regime is to slowly increase the freshwater forcing in the Northern Atlantic until a critical threshold is crossed: the stable AMOC state ceases to exist and the circulation collapses to the other stable state without an active AMOC in a bifurcation tipping event. Subsequently the forcing is reduced again until the collapsed state no longer exists and the AMOC recovers. The interval in forcing conditions between collapse and recovery is the AMOC hysteresis width and a nonzero width indicates the existence of multiple equilibria. Such AMOC hysteresis has been found in Earth system Models of Intermediate Complexity (Rahmstorf et al. 2005; Lenton et al. 2007) and global ocean models (Hofmann and Rahmstorf 2009). Full AMOC hysteresis simulations have also been performed with a low resolution atmosphere-ocean coupled general circulation model (FAMOUS) (Hawkins et al. 2011), and in a state-of-the-art global climate model (CESM) (van Westen and Dijkstra 2023).

The AMOC is identified as a tipping element in the climate system (Lenton et al. 2008). Based on early warning signals determined from historical AMOC reconstruction data (Caesar et al. 2018), the AMOC is believed to be heading towards the bifurcation point (Boers 2021). Although estimates have recently been provided when such a bifurcation point would be reached (Ditlevsen and Ditlevsen 2023), many uncertainties remain and the present-day AMOC state may be far from it. Therefore, what is more dangerous is a noise-induced transition, where the transition does not happen because a certain critical threshold was crossed, but due to the fast variability in the forcing ('noise'). Not only are there no reliable early warn-

Corresponding author: Jelle Soons j.soons@uu.nl

ing signals for a noise-induced transition as opposed to a bifurcation-induced one (Ditlevsen and Johnsen 2010), but more so that the latter can only occur close to the bifurcation point whereas the former can take place as long as the AMOC is multi-stable. This is arguably the case for the present-day AMOC. Based on observations of the AMOC induced freshwater transport at the southern boundary of the Atlantic, the present-day AMOC is thought to be in a multiple equilibrium regime (Weijer et al. 2019). The reliability of this transport as an indicator for multi-stability is however contentious (Jackson and Wood 2018). Several stochastic models of the AMOC have been developed with stochastic freshwater forcing and the statistics of their noise-induced transitions have been analysed (Cessi 1994; Timmermann and Lohmann 2000) and recently even a noise-induced long-time weakening of the AMOC has been found in a global model (Romanou et al. 2023).

However, as there is no observational evidence for an AMOC transition over the historical period, a noise-induced transition is expected to be a rare event and simple Monte Carlo techniques are unsuitable for such low-probability events. Rare event techniques have been used to determine such transitions probabilities in box models (Castellana et al. 2019; Jacques-Dumas et al. 2024). However, apart from such probabilities, information on the most likely path of such an AMOC transition is also desired. From this, likely new observable early warning signals can be determined of an AMOC collapse.

In this paper, we use a technique from Large Deviation Theory (LDT) to directly compute the most likely transition path in the low-noise limit of a stochastic model, i.e. the instanton. This is achieved by minimizing the Freidlin-Wentzell action (Freidlin and Wentzell 1998), transforming a rare transition sampling problem into a deterministic one. Minimizing this action entails that we maximize the probability of the applied noise forcing under the constraints that a transition occurs. The resulting path (the instanton) allows us to analyse the mechanisms of a noise-induced transition. Note that the forcing implies the path (and vice-versa) so with the most likely path comes the optimal forcing. This associated forcing is just sufficient enough to attain the rare event. In other scientific fields instantons have already been used to analyze transitions (Grafke et al. 2015; Grafke and Vanden-Eijnden 2019; Woillez and Bouchet 2020; Schorlepp et al. 2022; Blyuss and Kyrychko 2023). We apply the technique here to compute the instanton for an AMOC collapse and recovery in the box model from Wood et al. (2019), where stochastic freshwater forcing is added. We will present the paths for an AMOC collapse and recovery that have the most probable freshwater forcing needed to achieve these transitions.

In section 2, a brief introduction to the Freidlin-Wentzell theory of Large Deviations is provided and the algorithm used to compute the instanton is presented. Then, section

3 discusses the stochastic version of the box model from Wood et al. (2019) together with the assumptions on the applied freshwater noise. Section 4 presents results on the instantons and the accompanying optimal forcings found for an AMOC collapse and recovery for the stochastic box model. In section 5, the distribution of this stochastic freshwater forcing over the boxes in the model is altered to study the effects of different freshwater forcing on the most likely AMOC collapse and recovery. Furthermore, the instanton trajectories are compared to the trajectories resulting from a standard deterministic hosing experiment. Finally, in section 6, a summary and discussion of the results follow.

2. Theory

a. Freidlin-Wentzell Theory of Large Deviations

Consider a dynamical system with state vector X_t in \mathbb{R}^d , forced by small random perturbations which are white in time and additive Gaussian. The noise amplitude scales with smallness-parameter ϵ . The system can then be described by the stochastic differential equation (SDE):

$$dX_t = f(X_t) dt + \sqrt{\epsilon} \sigma dW_t, \quad t \geq 0, \quad (1)$$

where $f : \mathbb{R}^d \rightarrow \mathbb{R}^d$ is the deterministic drift, $a = \sigma \sigma^T$ the noise covariance with $\sigma \in \mathbb{R}^{d \times k}$, and W_t a k -dimensional Wiener process. For simplicity we take a to be independent of the system's state (although this theory can be generalized to include multiplicative noise), but it is not assumed that a is invertible, i.e. the noise can be degenerate. Of interest are situations where the stochastic process (1) realizes a certain event, say a transition within time T starting at $X_0 = x$ and ending at $X_T = y$ for certain points in phase space $x, y \in \mathbb{R}^d$ and time T . These events might be impossible in the deterministic setting ($\epsilon = 0$) but can occur in the presence of noise ($\epsilon > 0$), although they become increasingly rare in the low-noise limit ($\epsilon \rightarrow 0$).

LDT provides the rate at which this probability decays to zero with ϵ . The probability of observing a sample path close to a function $\phi : [0, T] \rightarrow \mathbb{R}^d$ ($t \mapsto \phi(t)$) behaves as:

$$\mathbb{P} \left[\sup_{t \in [0, T]} \|X_t - \phi(t)\| < \delta \right] \asymp \exp \left[-S_T[\phi] / \epsilon \right] \quad (2)$$

for sufficiently small $\delta > 0$, and where \asymp denotes the log-asymptotic equivalence. The functional $S_T[\phi]$ is the Freidlin-Wentzell action and is defined as

$$S_T[\phi] = \frac{1}{2} \int_0^T \langle \dot{\phi}(t) - f(\phi(t)), a^{-1}(\dot{\phi}(t) - f(\phi(t))) \rangle dt \quad (3)$$

if the integral converges, otherwise $S_T[\phi] = \infty$. Here, $\langle \cdot, \cdot \rangle$ is the standard Euclidean inner product which induces the norm $\|\cdot\|$, and a^{-1} the inverse of the covariance matrix

(Freidlin and Wentzell 1998). More technical constraints are that $f(\phi)$ needs to be Lipschitz-continuous in ϕ , and the path $\phi(t)$ needs to be absolutely continuous in time t . Moreover, if a is singular then a^{-1} can be replaced by the Moore-Penrose inverse provided a positive-definite $a^{1/2}$ exists, and provided $\phi - f(\phi)$ is in the image of a (Puhalskii 2004).

The important consequence of (2) is that in the limit of $\epsilon \rightarrow 0$ the trajectory $\phi^*(t)$ with the smallest action becomes the least unlikely trajectory to realize the rare event, and all sample paths conditioned on the rare event ($\phi(0) = x$, $\phi(T) = y$) will concentrate around ϕ^* . More precisely:

$$\phi^*(t) = \underset{\{\phi(0)=x, \phi(T)=y\}}{\operatorname{arg\,min}} S_T[\phi] \quad (4)$$

is the instanton (or maximum likelihood pathway), and for $\delta > 0$ sufficiently small

$$\lim_{\epsilon \rightarrow 0} \mathbb{P} \left[\sup_{t \in [0, T]} \|X_t - \phi^*(t)\| < \delta \mid X_0 = x, X_T = y \right] = 1.$$

So the objective here is to compute the instanton ϕ^* i.e. the minimizing path of the Freidlin-Wentzell action functional under the constraints that this is a transition path. Simply speaking, it is the path whose associated forcing is the most likely to occur of all possible forcings that cause a transition in a time T .

b. Hamiltonian Principle

The minimization problem (4) is a common problem within classical mechanics (Taylor 2005) and so similar methods can be applied. The Lagrangian of (4) is

$$\mathcal{L}(\phi, \dot{\phi}) = \frac{1}{2} \langle \dot{\phi}(t) - f(\phi(t)), a^{-1}(\dot{\phi}(t) - f(\phi(t))) \rangle$$

and assuming convexity of $\mathcal{L}(\phi, \dot{\phi})$ in $\dot{\phi}$, a Hamiltonian can be formulated by taking its Fenchel-Legendre transform (Grafke and Vanden-Eijnden 2019)

$$\mathcal{H}(\phi, \theta) = \sup_y (\langle \theta, y \rangle - \mathcal{L}(\phi, y)),$$

where θ is the conjugate momentum defined as

$$\theta = \frac{\partial \mathcal{L}(\phi, \dot{\phi})}{\partial \dot{\phi}}.$$

Hence the Hamiltonian is

$$\mathcal{H}(\phi, \theta) = \langle f(\phi), \theta \rangle + \frac{1}{2} \langle \theta, a\theta \rangle \quad (5)$$

and so the Hamiltonian equations of motion, i.e. the instanton equations follow:

$$\begin{cases} \dot{\phi} &= \nabla_{\theta} \mathcal{H}(\phi, \theta) = f(\phi) + a\theta \\ \dot{\theta} &= -\nabla_{\phi} \mathcal{H}(\phi, \theta) = -(\nabla f(\phi))^T \theta \end{cases} \quad (6)$$

with boundary conditions $\phi(0) = x$ and $\phi(T) = y$. Solving these equations yields the instanton $\phi^*(t)$. Note that for this path the Hamiltonian is conserved. An advantage of this approach is that the covariance matrix a does not need to be inverted. A disadvantage is that for one first-order equation two boundary conditions are known, while for the conjugated equation there are none. A naive solution would be to guess $\theta(0)$ such that $\phi(T)$ is close to y i.e. a shooting method, which is unpractical in higher dimensions. So to solve (6) we use the Augmented Lagrangian method (Hestenes 1969; Schorlepp et al. 2022), see Appendix A for details.

3. Model

The ocean model used was originally introduced by Wood et al. (2019), and is chosen since it is calibrated to the FAMOUS-model (Smith et al. 2008; Smith 2012)). They show that this simple box model encapsulates the physics of the more complicated AOGCM. It represents the World Ocean in five boxes, see figure 1. Each box represents large contiguous regions of the global ocean, corresponding to large-scale water mass structures. The T box represents the Atlantic thermocline; the N box is the North Atlantic Deep Water (NADW) formation region and Arctic region; the B box is the southward propagating NADW and its upwelling in the Southern Ocean as Circumpolar Deep Water; the S box is the fresh Southern Ocean near-surface waters and their return into the Atlantic as Antarctic Intermediate Water, and lastly the IP box represents the Indo-Pacific thermocline. The calibration entails that the box model reproduces the decadal means of salinities, temperatures, volumes and transports of these mean water masses observed in the stable pre-industrial climate state of the AOGCM. The boxes have salinities denoted by S_N , S_T , S_S , S_B and S_{IP} respectively, along with fixed volumes V_N , V_T , V_S , V_B and V_{IP} .

a. Formulation

It is assumed that density variations in the boxes are solely due to changes in the boxes' salinity and in the temperature of the northern box. The other boxes' temperatures are taken to be constant. The following volume fluxes occur between the boxes: downwelling in the North Atlantic (and hence AMOC strength) q that transports salt between the T , N and B box, a cold water path (CWP) that returns a fraction γ of the AMOC from the B box via the S box to the T box, representing the return flow via the Drake Passage, and a warm water path (WWP) that returns

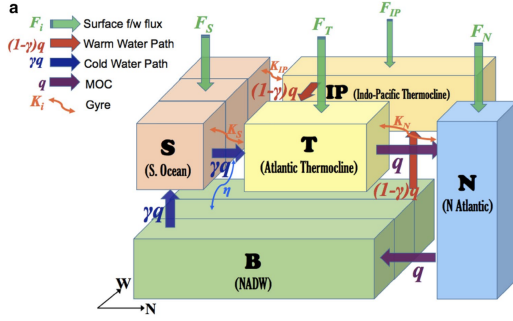


FIG. 1: Sketch of the box model, from Wood et al. (2019).

the AMOC's remaining fraction $1 - \gamma$ from the B box via the IP box to the T box, representing the return flow via the Agulhas leakage. It is assumed that the overturning circulation is linear dependent on the density difference of the N and S boxes:

$$q = \lambda(\alpha(T_S - T_N) + \beta(S_N - S_S)),$$

with α and β the thermal and haline compressibility, λ a hydraulic coefficient, and T_S the fixed mean temperature of the S box. Additionally, T_N is the mean temperature of the northern box obeying

$$T_N = \mu q + T_0.$$

Here T_0 is a fixed baseline temperature, and $\mu > 0$ the fixed heat transport coefficient. This represents the northward transport of heat by the overturning circulation. Combining the latter two equations yields:

$$q = \kappa(\alpha(T_S - T_0) + \beta(S_N - S_S)),$$

$$\text{where } \kappa = \frac{\lambda}{1 + \alpha\lambda\mu}$$

eliminating T_N from the equations and hence the state of the dynamical model is completely characterized by the boxes' five salinities.

The other salinity transports are due to the wind-driven subtropical gyres, captured by the coefficients K_N , K_S and K_{IP} for the exchange between T and N , T and S , and IP and S respectively. Furthermore, the coefficient η captures the mixing between B and S . The atmospheric fluxes are denoted by F_i for the flux into box i .

The stochastic extension of the Wood et al. (2019) model is given by the equations:

$$V_N \frac{dS_N}{dt} = q(\theta(q)(S_T - S_N) - \theta(-q)(S_B - S_N)) + K_N(S_T - S_N) - F_N S_0 + A_N S_0 \tilde{\eta} \quad (7a)$$

$$V_T \frac{dS_T}{dt} = q(\theta(q)(\gamma S_S + (1 - \gamma)S_{IP} - S_T) - \theta(-q)(S_N - S_T)) + K_S(S_S - S_T) - F_T S_0 + A_T S_0 \tilde{\eta} \quad (7b)$$

$$V_S \frac{dS_S}{dt} = \gamma q(\theta(q)(S_B - S_S) - \theta(-q)(S_T - S_S)) + K_{IP}(S_{IP} - S_S) + K_S(S_T - S_S) + \eta(S_B - S_S) - F_S S_0 + A_S S_0 \tilde{\eta} \quad (7c)$$

$$V_{IP} \frac{dS_{IP}}{dt} = (1 - \gamma)q(\theta(q)(S_B - S_{IP}) - \theta(-q)(S_T - S_{IP})) + K_{IP}(S_S - S_{IP}) - F_{IP} S_0 + A_{IP} S_0 \tilde{\eta} \quad (7d)$$

$$V_B \frac{dS_B}{dt} = q(\theta(q)(S_N - S_B) - \theta(-q)(\gamma S_S + (1 - \gamma)S_{IP} - S_B)) + \eta(S_S - S_B) \quad (7e)$$

where S_0 is a baseline salinity value and $\theta(x)$ the Heaviside function. The stochastic freshwater flux $\tilde{\eta}(t)$ is modelled as a zero-mean Gaussian white noise process with correlation function $\mathbb{E}(\tilde{\eta}(t)\tilde{\eta}(t')) = \nu\delta(t - t')$. The parameters A_i indicate what fraction of $\tilde{\eta}$ enters or exits box i .

The total salinity C is

$$C = V_N S_N + V_T S_T + V_S S_S + V_{IP} S_{IP} + V_B S_B, \quad (8)$$

and using (7), it follows that

$$\frac{dC}{dt} = -(F_N + F_T + F_S + F_{IP})S_0 + (A_N + A_T + A_S + A_{IP})S_0 \tilde{\eta}.$$

The total salinity is conserved, so it is demanded that

$$F_N + F_T + F_S + F_{IP} = 0, \\ A_N + A_T + A_S + A_{IP} = 0.$$

Using (8), the differential equation (7e) is replaced by:

$$S_B = \frac{1}{V_B}(C - V_N S_N - V_T S_T - V_S S_S - V_{IP} S_{IP})$$

with C the basin's total (fixed) salinity.

b. Non-dimensional equations

The non-dimensional salinities ϕ_i of the boxes are introduced, together with non-dimensionalized volumes V_i :

$$S_N = S_0 \phi_1 \quad V_N = V_0 V_1 \\ S_T = S_0 \phi_2 \quad V_T = V_0 V_2 \\ S_S = S_0 \phi_3 \quad V_S = V_0 V_3$$

$$\begin{aligned} S_{IP} &= S_0\phi_4 & V_{IP} &= V_0V_4 \\ S_B &= S_0\phi_5 & V_B &= V_0V_5 \end{aligned}$$

and furthermore time t is non-dimensionalized as $t = t_d\tau$, with notation $\dot{\phi}_i = \frac{d\phi_i}{d\tau}$. The non-dimensional model equations then become:

$$\begin{aligned} \dot{\phi}_1 &= \frac{t_d}{V_0} \frac{1}{V_1} \left(q[\theta(q)(\phi_2 - \phi_1) - \theta(-q)(\phi_5 - \phi_1)] \right. \\ &\quad \left. + K_N(\phi_2 - \phi_1) - F_N \right) + \frac{t_d}{V_0} \frac{A_N}{V_1} \sqrt{v}\zeta \end{aligned} \quad (9a)$$

$$\begin{aligned} \dot{\phi}_2 &= \frac{t_d}{V_0} \frac{1}{V_2} \left(q[\theta(q)(\gamma\phi_3 + (1-\gamma)\phi_4 - \phi_2) \right. \\ &\quad \left. - \theta(-q)(\phi_1 - \phi_2)] + K_S(\phi_3 - \phi_2) \right. \\ &\quad \left. + K_N(\phi_1 - \phi_2) - F_T \right) + \frac{t_d}{V_0} \frac{A_T}{V_2} \sqrt{v}\zeta \end{aligned} \quad (9b)$$

$$\begin{aligned} \dot{\phi}_3 &= \frac{t_d}{V_0} \frac{1}{V_3} \left(\gamma q[\theta(q)(\phi_5 - \phi_3) - \theta(-q)(\phi_2 - \phi_3)] \right. \\ &\quad \left. + K_{IP}(\phi_4 - \phi_3) + K_S(\phi_2 - \phi_3) + \eta(\phi_5 - \phi_3) - F_S \right) \\ &\quad + \frac{t_d}{V_0} \frac{A_S}{V_3} \sqrt{v}\zeta \end{aligned} \quad (9c)$$

$$\begin{aligned} \dot{\phi}_4 &= \frac{t_d}{V_0} \frac{1}{V_4} \left((1-\gamma)q[\theta(q)(\phi_5 - \phi_4) - \theta(-q)(\phi_2 - \phi_4)] \right. \\ &\quad \left. + K_{IP}(\phi_3 - \phi_4) - F_{IP} \right) + \frac{t_d}{V_0} \frac{A_{IP}}{V_4} \sqrt{v}\zeta \end{aligned} \quad (9d)$$

where $\zeta(t)$ is a unit-variance white noise process and the (dimensional) AMOC strength is written as

$$q = \kappa(\alpha(T_S - T_0) + \beta S_0(\phi_1 - \phi_3)) \quad (10)$$

and non-dimensionalized S_B follows from salinity conservation

$$\phi_5 = \left(\frac{C}{V_0 S_0} - V_1\phi_1 - V_2\phi_2 - V_3\phi_3 - V_4\phi_4 \right) / V_5.$$

From now on t is again used, but now to denote the non-dimensional time.

The system of non-dimensionalized equations is rewritten as an Itô stochastic differential equation (Mikosch 1998):

$$d\phi_t = f(\phi_t) dt + \sqrt{\epsilon} \sigma dW_t \quad (11)$$

where $\phi_t = (\phi_1(t), \phi_2(t), \phi_3(t), \phi_4(t))^T$ is the state vector, and the deterministic parts of the evolution equations are $f(\phi) = (f_1(\phi), f_2(\phi), f_3(\phi), f_4(\phi))^T$. Furthermore, the noise amplitude is given by $\sqrt{\epsilon} = \frac{t_d}{V_0} \sqrt{v}$ and

$$\sigma = (A_N/V_1, A_T/V_2, A_S/V_3, A_{IP}/V_4)^T$$

acts on the 1-dimensional Wiener process. The system has degenerate noise: one degree of stochastic freedom is acting on the process $\phi_t \in \mathbb{R}^4$.

The parameter values (V_i 's, F_i 's, K_i 's, T_S , T_0 , μ , λ , η and γ) are taken from the calibration to the FAMOUS_B-model (Wood et al. 2019), see Table B1 in Appendix B. The total salinity C is found using the salinity values from Alkhuayon et al. (2019). For these values the deterministic model has two stationary stable points, an ON and OFF-state of the AMOC ($q \leq 0$) and an unstable saddle state (Alkhuayon et al. 2019). In the ON-state ($q > 0$) downwelling occurs in the north, and the resulting flow flows southward along the bottom before it returns to the Atlantic thermocline via either the Southern Ocean or the Indo-Pacific thermocline. In the OFF-state these flows are reversed, and upwelling occurs in the Northern Atlantic ($q < 0$). So states ϕ_{ON} and ϕ_{OFF} represent an active and collapsed AMOC respectively. They are found numerically using a root finding function, the dogleg method (Nocedal and Wright 1999), to $f: \mathbb{R}^4 \rightarrow \mathbb{R}^4$.

c. Instanton Equations

Recall that we want to compute the instantons for an AMOC collapse ($\phi_{ON} \rightarrow \phi_{OFF}$) and recovery ($\phi_{OFF} \rightarrow \phi_{ON}$) in model (11). So we need $f(\phi)$ to be Lipschitz-continuous in ϕ . We did this, by approximating the Heaviside function by $\theta(x) \approx (\text{erf}(x/\epsilon_\theta) + 1)/2$, where erf is the error function, for small $\epsilon_\theta = 10^{-10}$. The error caused by this approximation is assumed to be negligible.

Two assumptions were made of the freshwater noise: (i) the noise is white in time, and (ii) this noise is small. To justify (ii), estimating the noise amplitude can be done in a similar way as Castellana et al. (2019). The parameter ϵ is estimated by using the annual $P - E$ (precipitation minus evaporation) time series in the Atlantic Ocean, assuming that this represents the inter annual variability of freshwater perturbations relevant for the AMOC strength. Using the same time series, the ERA-Interim Archive at ECMWF (Dee et al. 2011), it is found for its variance that $\sqrt{v} \sim 0.0175 \pm 0.0025 \text{ Sv}$. Hence $\epsilon \sim 0.0055 \pm 0.0008$. This is in the regime of small noise, as for $\sqrt{v} \sim 0.07 \text{ Sv}$ typically no transition occurs even after 10^6 years, while a transition usually does not take longer than 35 years. Assumption (i) is harder to justify as the annual freshwater perturbation series might be auto-correlated, especially under climate change. However, the white noise assumption is still made to keep the model analysis relatively simple.

Applying the equations from section 2 to the stochastic box model yields the Lagrangian

$$\mathcal{L}(\phi, \dot{\phi}) = \frac{1}{2\|\sigma\|^4} \sum_{i,j=1}^4 \sigma_i \sigma_j (\dot{\phi}_i - f_i(\phi)) (\dot{\phi}_j - f_j(\phi))$$

with conjugate momentum $\theta : [0, T] \rightarrow \mathbb{R}^4$

$$\theta_i(t) = \frac{\sigma_i}{\|\sigma\|^4} \sum_{j=1}^4 \sigma_j (\dot{\phi}_j(t) - f_j(\phi_j(t))) \quad \text{for } 1 \leq i \leq 4$$

and hence the Hamiltonian for this minimization problem is

$$\mathcal{H}(\phi, \theta) = \langle f(\phi), \theta \rangle + \frac{1}{2} \|\sigma\theta\|^2.$$

Therefore the equations for the instanton from ϕ_{start} to ϕ_{end} within a time interval $[0, T]$ are:

$$\begin{cases} \dot{\phi}(t) = f(\phi(t)) + \sigma \langle \sigma, \theta(t) \rangle \\ \dot{\theta}(t) = -(\nabla f(\phi(t)))^T \theta(t) \\ \text{with } \phi(0) = \phi_{\text{start}} \text{ and } \phi(T) = \phi_{\text{end}}. \end{cases} \quad (12)$$

As the stochastic forcing is just a one-dimensional Wiener process, all deviations from the deterministic system are the same in every direction up to a scaling factor σ_i^{-1} , and one can define:

$$\xi(t) = (\dot{\phi}_i(t) - f_i(\phi(t))) / \sigma_i \quad \text{for } 1 \leq i \leq 4 \\ = \langle \sigma, \theta(t) \rangle$$

which reduces the previously mentioned relationships to:

$$\mathcal{L}(\xi) = \frac{1}{2} \xi^2 \quad (13a)$$

$$\mathcal{H}(\phi, \xi) = \frac{\langle f(\phi), \sigma \rangle}{\|\sigma\|^2} \xi + \frac{1}{2} \xi^2. \quad (13b)$$

The Lagrangian shows trivially that the most likely path is the one that minimizes the absolute total applied freshwater noise, while the Hamiltonian implies that to any freshwater perturbation the system ϕ responds with salinity changes in all boxes with proportionality factors $\sigma_i / \|\sigma\|^2$. We will obtain the path ϕ and accompanying forcing ξ that minimize this Lagrangian and do not vary the Hamiltonian – provided that this path is a transition.

4. Results: AMOC Transitions

a. Instantons

The instanton for an AMOC collapse from ϕ_{ON} to ϕ_{OFF} and its reverse (the ‘anti-instanton’) are computed for the noise parameters $(A_N, A_T, A_S, A_{IP})^T = (0.070, 0.752, -0.257, -0.565)$ which follow from the same calibration to the FAMOUS_B model (Wood et al. 2019). So freshwater goes into boxes N and T , and as compensation freshwater is extracted from boxes S and IP . This conserves the total salinity and so ϕ_{ON} and ϕ_{OFF} do not change during the hosing process. The equations (12) are solved using the discussed Augmented Lagrangian method, where explicit Euler is used for time integration

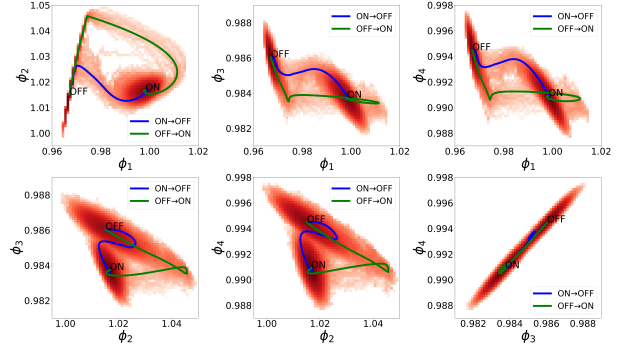


FIG. 2: Instantons from ϕ_{ON} to ϕ_{OFF} (blue) and vice versa (anti-instantons, green) in several salinity spaces (ϕ_i, ϕ_j) , together with a histogram of multiple realizations of the model for noise level $\epsilon \sim 0.035$ ($\sqrt{v} \sim 0.11\text{Sv}$) (red), using a logarithmic scale.

with time step $\Delta t = 0.05$. The instantons $\phi(t)$ are terminated once $\|\phi(T) - \phi_{\text{end}}\| < 10^{-5}$. For different values of $30 < T < 100$ the trajectory of the instanton is just translated in time without any significant change in behavior. Moreover the average times of a realization to transit from the ON-basin (defined by $q > 14\text{ Sv}$) to the OFF-basin (defined by $q < -4.5\text{ Sv}$) and vice versa level off for smaller noise levels (tested down to $\epsilon \sim 0.035$) at $T = 17$ and $T = 32$ for the collapse and recovery respectively. Hence $T = 32$ is sufficient to capture the relevant instanton behavior for both transition directions.

In the limit of large T the instantons are expected to cross from one basin to the other via the saddle present in the model. We do not consider these instantons to be representative of a typical transition, since the realizations here tend to avoid the saddle, which is an issue discussed in Börner et al. (2023).

In addition to the instanton trajectory $\phi(t)$, the associated optimal freshwater noise forcing $\xi(t)$ also follows from the optimization procedure (12) and is analyzed below. In Fig. 2, the resulting instantons are shown in several projected phase spaces (ϕ_i, ϕ_j) together with multiple realized transitions of the model. It shows that the instantons lie at the centre of these transitions, as they should be according to theory, and this serves as their verification. We will analyse the mechanisms underlying the behavior of these instantons in the following subsections.

b. Dynamics of Collapse & Recovery

In Fig. 3 the dimensional instantons of the collapse and recovery are shown together with their AMOC strength q for a time frame $t \in [0, 32]$ years. The insets show the accompanying dimensional stochastic freshwater forcings into boxes N and T , which are computed as $-\frac{V_0}{t_d} (V_1 \sigma_1 + V_2 \sigma_2) \xi(t)$. A positive sign indicates net freshwater going

into these boxes. Mainly the salinities in the N and T boxes change, while those in the other boxes only vary marginally. Wood et al. (2019) observed this already, and suggested a possible reduction of the model without S and IP . In those boxes advection by the density-induced flow plays a lesser role, and their salinities are mainly controlled by the atmospheric fluxes and the Indo-Pacific gyre transport. Hence the tipping of the AMOC affects these boxes to a lesser extent than the N and T boxes.

The dynamics of the AMOC collapse and recovery can be captured by a reduced model. We assume ϕ_3 (i.e. S_S) is constant and that A_N is negligible. The former assumption is justified as it can be deduced from figure 3, while the latter is justified since the hosing transport into box N is several orders of magnitude smaller than the other transports. Now for $q > 0$ it holds that:

$$\begin{aligned}\dot{q} &= \kappa\beta S_0 \dot{\phi}_1 \\ &= \kappa\beta S_0 \frac{t_d}{V_0 V_1} \left[(K_N + q)(\phi_2 - \phi_1) - F_N \right]\end{aligned}$$

then substituting the relation $\phi_1(q)$ derived directly from (10) yields

$$\dot{q}_{\text{ON}}(q, \phi_2) = A_{\text{ON}} q^2 + B_{\text{ON}} q + C_{\text{ON}} \quad (14)$$

with

$$\begin{aligned}A_{\text{ON}} &= -\frac{t_d}{V_0 V_1} \\ B_{\text{ON}} &= \frac{t_d}{V_0 V_1} (\kappa\beta S_0 (\phi_2 - \phi_3) - K_N + \kappa\alpha (T_S - T_0)) \\ C_{\text{ON}} &= \frac{t_d}{V_0 V_1} \kappa\beta S_0 \left(K_N \left(\phi_2 + \frac{\alpha (T_S - T_0)}{\beta S_0} - \phi_3 \right) - F_N \right).\end{aligned}$$

A similar derivation can be done for the AMOC dynamics as $q < 0$ which leads to

$$\dot{q}_{\text{OFF}}(q, \phi_2) = A_{\text{OFF}} q^2 + B_{\text{OFF}} q + C_{\text{OFF}} \quad (15)$$

with

$$\begin{aligned}A_{\text{OFF}} &= \frac{t_d}{V_0 V_1} \\ B_{\text{OFF}} &= \frac{t_d}{V_0 V_1} (\kappa\beta S_0 (\phi_3 - \phi_5) - K_N - \kappa\alpha (T_S - T_0)) \\ C_{\text{OFF}} &= \frac{t_d}{V_0 V_1} \kappa\beta S_0 \left(K_N \left(\phi_2 + \frac{\alpha (T_S - T_0)}{\beta S_0} - \phi_3 \right) - F_N \right).\end{aligned}$$

The evolution of $\dot{q}(q, \phi_2)$ along the instantons is depicted in Fig. 4.

1) COLLAPSE

Initially the system is in equilibrium ϕ_{ON} , which is a stable root of $\dot{q}_{\text{ON}}(q, \phi_2) = 0$ (Fig. 4a). This right root is stable, since a small increase (decrease) in q would cause the N box to become saltier (fresher), which is mitigated by

a decrease (an increase) in Northern gyre transport that in turns freshens (salinifies) the Northern box, which finally weakens (strengthens) the AMOC. This stable root will continue to exist as long as the discriminant of $\dot{q}_{\text{ON}}(q, \phi_2)$ stays positive, i.e. $D_{\text{ON}} = B_{\text{ON}}^2 - 4A_{\text{ON}}C_{\text{ON}} > 0$. It can be derived that this condition is equivalent to

$$\phi_2 - \phi_3 > r(T_S - T_0) - k_N + 2\sqrt{f_N} \approx 0.0494 \quad (16)$$

$$\text{or } \phi_2 - \phi_3 < r(T_S - T_0) - k_N - 2\sqrt{f_N} \approx -0.0477$$

$$\text{where } k_N = \frac{K_N}{\kappa\beta S_0}, r = \frac{\alpha}{\beta S_0} \text{ and } f_N = \frac{F_N}{\kappa\beta S_0}$$

where only the first inequality is considered as $\phi_2 - \phi_3 < 0$ does not happen. Looking at this inequality it follows that a larger Northern gyre strength, a warmer Southern box or a smaller atmospheric flux into box N would all enlarge this range for $\phi_2 - \phi_3$. This follows directly from the facts that the Northern gyre serves as a stabilizing mechanism (as just described) whereas a warmer South would decrease the density of the S box (so increasing q) and F_N is a destabilizing freshening into N . The role of κ is ambiguous, as a stronger feedback mechanism would stabilize the AMOC via the thermal circulation, and destabilize it via the haline circulation (the salt-advection feedback).

The AMOC collapse paradoxically starts off with an increase in its strength. Initially the optimal hosing scheme salinifies the northern N and the thermocline T boxes, while the other salinities change marginally as their volumes are larger. The increase in S_N causes an increase in q , peaking at roughly $t \approx 10.8$ years with $q \approx 16.3\text{Sv}$. This short salinification pulse ends already at $t \approx 12$ years, and q is back at its original level. However, the current state is a transient state (i.e. non-equilibrium), with box T slightly fresher ($\mathcal{O}(10^{-3})$), while the others are marginally saltier ($\mathcal{O}(10^{-4})$) compared to the equilibrium ON-state. So the salt is redistributed. The salinity difference $S_N - S_S$, which determines the AMOC strength, is still the same, while $S_T - S_N$ has decreased. When applying freshwater to the Northern boxes the salinity difference $S_N - S_S$ drops, and S_N cannot as easily be restored via the gyre since $S_T - S_N$ is lower. This also follows from (16): as $\phi_2 - \phi_3$ decreases, the discriminant D_{ON} will decrease, thus the distance between the two roots in Fig. 4a diminishes and the stability region for an ON-state narrows. This destabilizing effect of the initial AMOC strengthening is quantified by computing the probabilities of a collapse within 100 years for trajectories starting in the standard ON-state and in this destabilized state. These probabilities are estimated using Monte Carlo simulations for various (unrealistically high) noise levels $\sqrt{v} \in \{0.11, 0.10, 0.09, 0.08\}\text{Sv}$. They are $\{(6.4 \cdot 10^{-3}, 6.5 \cdot 10^{-3}), (1.9 \cdot 10^{-3}, 2.1 \cdot 10^{-3}), (3 \cdot 10^{-4}, 4 \cdot 10^{-4}), (2 \cdot 10^{-5}, 4 \cdot 10^{-5})\}$ for trajectories starting in the ON-state and in the destabilized state respectively. Hence this probability is only slightly larger in the destabi-

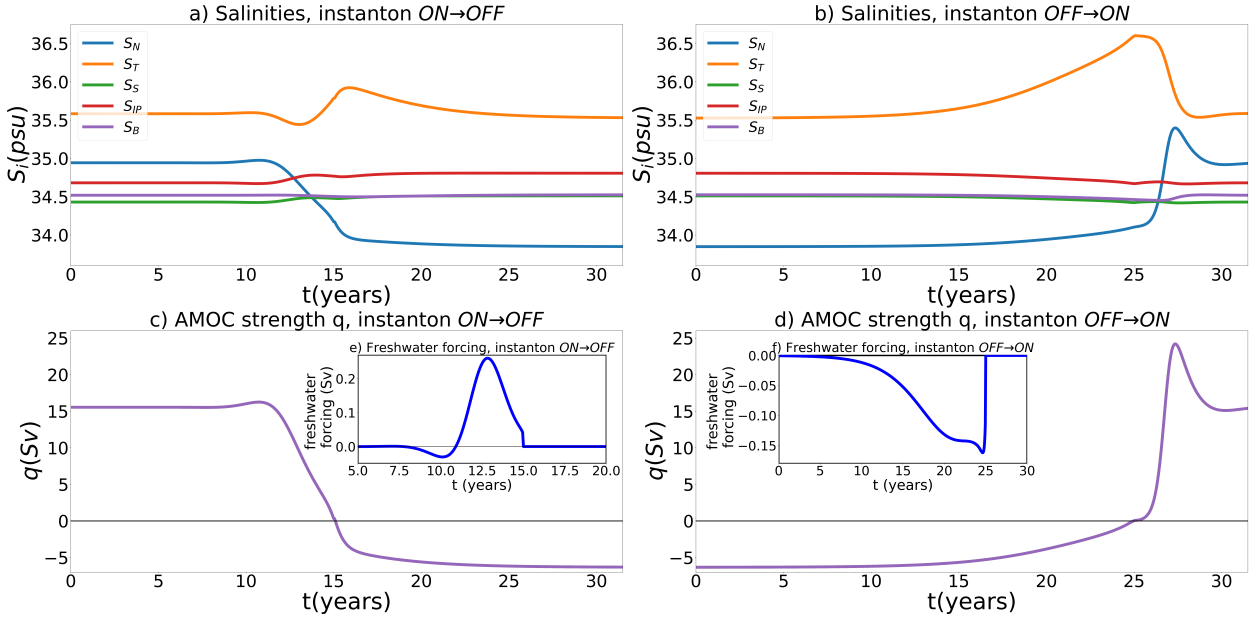


FIG. 3: Instantons from the ON-state to the OFF-state (left) and reverse (right) shown as the five salinities (top) and AMOC strength (bottom), with the optimal freshwater forcing as insets. The salinities S_N , S_T , S_S , S_{IP} and S_B are indicated by blue, yellow, green, red and purple respectively.

lized state than in the ON-state for the various noise levels. However, the ratio of the respective probabilities increases for smaller noise, and hence especially in the low-noise regime this initial strengthening of the AMOC increases the collapse probability significantly.

After this initial strengthening, a relatively large freshwater pulse is added to T during $t \in (11, 15)$ years causing its salinity to drop. Now fresher water is transported northward by the AMOC, and so S_N drops too. This in turn causes the AMOC strength to decrease, so less saline water is transported northward by it, which decreases S_N even further: the salt-advection feedback. This freshening of N is partly offset by salt transport by the Northern gyre. Note that this also follows from (14): for increased ϕ_2 the stable root disappears and $\dot{q}_{ON} < 0$ for all $q > 0$ (Fig. 4b). Using (16) and taking $\phi_3 \approx \phi_{ON,3}$ then no roots exist for $\phi_2 < 1.0146$ ($S_T < 35.5$). During this time the salinities of S and IP increase due to the pulse of salinity, and remain at this level with an increased Indo-Pacific gyre transport.

The freshwater pulse peaks at $t = 12$ years and then decreases. The T box is not freshened anymore and its salinity increases again due to the reduced advection of saline water to the north and of fresher water from the S and IP boxes. Apparently a fresher Atlantic thermocline is no longer needed to destabilize the AMOC. Its salinity even overshoots before it converges to its new stable $\phi_{OFF,2}$ state. As can be seen from figure 4c a stable ON-state exists again, but the current state of the AMOC is to the left of the unstable root and hence in the unstable

regime. The AMOC is now too weak to sustain itself as it cannot transport enough salt northward and even a saltier thermocline cannot save it. At the maximum value of $\phi_2 \approx 1.025$ ($S_T \approx 35.9$) the AMOC is still unstable ($\dot{q} < 0$) for $q < 2.9$ Sv.

In Fig. 4d the final phase of the collapse is depicted: a sharp freshwater pulse has put the AMOC into the unstable regime. It will continue to the OFF-regime ($q < 0$) and eventually collapse to the stable OFF-equilibrium at $q = -6$ Sv. Apparently it is more efficient to put the AMOC in this regime via a salinification and a subsequent freshwater pulse than via just one big freshwater pulse. Note that in this new regime ($q < 0$) there is only one stable root (Fig. 4e), so from now on it converges deterministically to this stable OFF-state and the freshwater forcing is no longer needed.

2) RECOVERY

As seen in figure 4e in the OFF-regime ($q < 0$) there is only one root (equilibrium), which is stable. The physical intuition here is that for a lower (higher) AMOC, more (less) salinity is transported from B to N , which salinifies (freshens) N and hence increases (decreases) the AMOC.

In order to restart the AMOC the N box needs to be more saline, which can only be achieved via Northern gyre transport from T and its increased salinity S_T . That is why ϕ_2 only occurs multiplied by the gyre coefficient K_N in (15). From this equation it can also be derived that there

will always be a stable attracting root in the range $q < 0$ unless

$$\phi_2 \geq \phi_3 + \frac{f_N}{k_N} - r(T_S - T_0) \approx 1.045. \quad (17)$$

For any higher S_T values, the gyre transport can salinify the N box enough for the AMOC to restart. From (17) it also follows that an increased gyre coefficient K_N or temperature difference would aid this recovery, whereas increasing S_S or the freshwater flux F_N would inhibit it.

So the salinities S_T and S_N (via the gyre transport) slowly increase until $S_T \approx 36.58$ ($\phi_2 \approx 1.045$). Meanwhile in the other boxes the salinity remains largely unchanged. As $S_N - S_S$ slowly increases, so does the AMOC strength, see Figs. 4f-g. Note that the AMOC remains close to the shifting stable root (the equilibrium).

The moment that the AMOC reverses, indeed at $S_T \approx 36.58$, there is no longer a attracting stable OFF-state. Suddenly a large salinity transport occurs from the T to the N box. Hence the salinity in the T box rapidly drops, while the opposite takes place in the Northern box. With this strong increase in S_N the AMOC strength also rises fast, and even overshoots above the level of the stable root $\dot{q}_{\text{ON}}(q, \phi_2) = 0$ (Fig. 4h). During the increase of the AMOC, the salinities in IP and S adjust with a decreased Indo-Pacific gyre transport.

From thereon the AMOC converges to the stable ON-state: the N box freshens and the T box salinifies via a reduced Northern gyre transport, with that the AMOC strength decreases to the stable ON-equilibrium at $q = 15\text{Sv}$ (Fig. 3d). Note that due to high salinity S_T just after $q > 0$ is attained, the basin of attraction of the stable root is huge, and so the system can reach this equilibrium without any additional forcing (Fig. 4i).

c. Sharp vs Sustained Forcing

There is a stark asymmetry between the collapse and the recovery of the AMOC. For the collapse a sharp pulse of freshwater is sufficient to get the system into the unstable regime from whereon it collapses due to its own dynamics. So the pulse already decreases before the actual collapse at $q = 0$. In the OFF-region there is no unstable regime, and the stable root has to be shifted with a sustained pulse of salinity until it is close to the AMOC restart at $q = 0$.

The differences between equations (14) and (15) are between the coefficients B_{ON} and B_{OFF} , and that $A_{\text{ON}} = -A_{\text{OFF}}$. The latter equation follows from the fact that for a too large AMOC ($|q| \rightarrow \infty$) it transports a lot of salinity out off N box to either B or T , and so S_N decreases again (note that $\phi_1 \sim -|q|\phi_1$). Hence $|\dot{q}| \sim -|q|^2$ prevents $|q|$ from exploding. The difference between the coefficients B_{ON} and B_{OFF} is more interesting as the thermocline's salinity appears in B_{ON} but not in B_{OFF} . This is because in the ON-regime the salinity S_N (and so the AMOC strength) is

also determined by the advective salinity transport from the thermocline (i.e. $q\phi_2$). In the OFF-regime only the gyre transport ($K_N\phi_2$) is present. Hence, in the ON-regime it is possible to use ϕ_2 to manipulate the AMOC to enlarge the unstable regime, whereas for the OFF-regime the B_{OFF} term cannot be altered.

Lastly, we consider the shape of the optimal forcings associated with the most likely transition paths. A sharp pulse is optimal to collapse the AMOC, and to recover a gradual (almost linear) increase in forcing has the highest probability. In both cases a certain salinity value S_T needs to be attained: for the collapse T needs to be fresh enough such that \dot{q}_{ON} has no roots, while for the recovery it needs to be saline enough to move the stable root to $q = 0$. Also for both cases there is a time penalty: the longer it takes to get to this S_T value the more of the input leaks away to other boxes. On the other hand, it should not be done too fast, because this requires high freshwater input values, which are unlikely. The additional leakages that occur when changing ϕ_2 are:

$$V_2 \frac{V_0}{t_d} \frac{\partial \phi_2}{\partial \phi_2} = -(K_N + K_S) - |q|$$

which are additional outpour via gyres, and varying outpour via advection. Now, $K_N + K_S \approx 10.9\text{Sv}$, and $|q| \approx 15.5\text{Sv}$ and $|q| \approx 6.3\text{Sv}$ in the stable ON and OFF-state respectively. So in the recovery, the additional outpour from the thermocline box is mainly via the gyres, especially as $|q| \rightarrow 0$. Therefore the additional salinity input during the recovery ideally grows linearly, since the leakage also grows linearly. However, for the collapse the decreased salinity transport out off the thermocline is dominated by the AMOC advection. As it diminishes, less salinity is transported out off the Atlantic thermocline and it becomes more saline, i.e. as $|q| \rightarrow 0$ the salinification rate $\dot{\phi}_2$ slows down with the freshening of box T . The evolution of the AMOC is non-linear due to salt-advection feedback and it can be heuristically concluded (as the shape of the optimal freshwater forcing cannot be analytically determined) that the loss of advective salinity transport is compensated by the surface freshwater input, and hence the initial shape of the optimal freshwater pulse is determined by the decrease of the AMOC.

5. Response to Surface Freshwater Forcing

a. Effect of Freshwater Forcing Locations

Following the Large Deviation Principle (LDP) the leading order term of the ratios of probabilities in the limit of small noise can be determined. Suppose one has paths $\phi_A(t)$ and $\phi_B(t)$ with Freidlin-Wentzell actions S_A and S_B

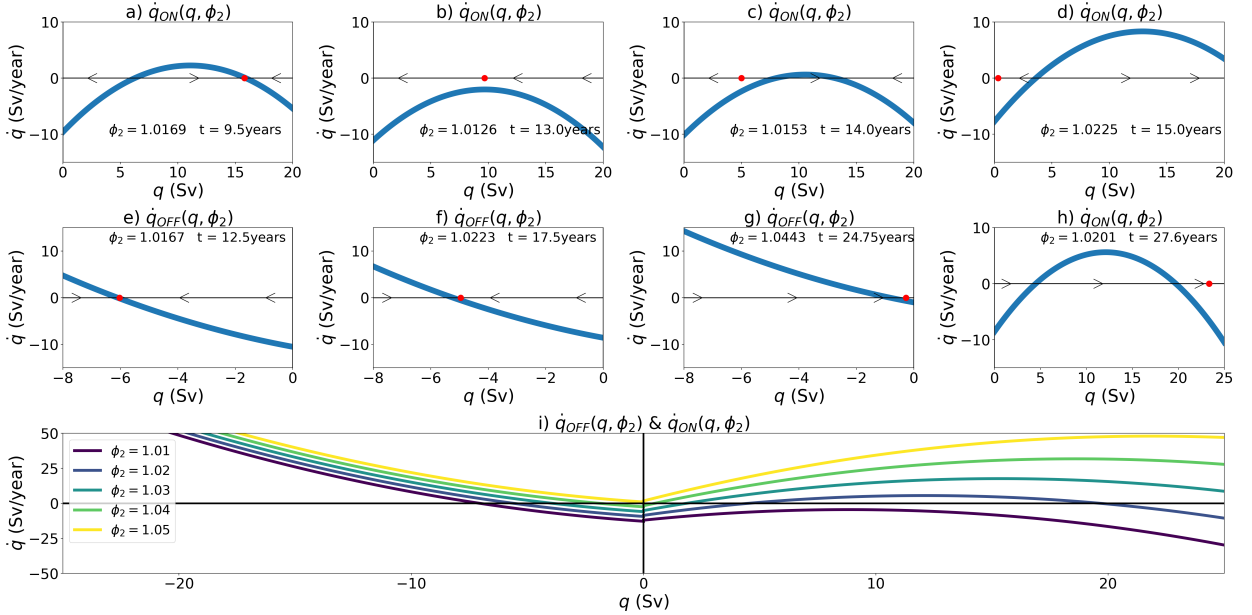


FIG. 4: Dynamics of the AMOC collapse (recovery) in the top (middle) figures: $\dot{q}(q, \phi_2)$ (blue) in the (\dot{q}, q) -plane with time t and salinity ϕ_2 values along each instanton added, and current AMOC strength q indicated by the red dot. The arrows on the q -axis indicate the sign of \dot{q} . Bottom figure *i*) shows complete $\dot{q}(q, \phi_2)$ curves for several $\phi_2 \in (1.01, 1.05)$.

respectively then their relative likelihood is

$$\frac{\mathbb{P}(\phi_B)}{\mathbb{P}(\phi_A)} \asymp \exp[(S_A - S_B)/\epsilon],$$

as long as ϕ_A and ϕ_B occur in systems like (1) with the same dimensions d and k and the same smallness parameter ϵ , see the derivation in Appendix C. Now the relative likelihood for the collapse and recovery of the AMOC can be determined: $S[\phi_{\text{ON} \rightarrow \text{OFF}}] = \frac{1}{2} \sum_t \xi_{\text{ON} \rightarrow \text{OFF}}^2 \Delta t = 0.00865$ and $S[\phi_{\text{OFF} \rightarrow \text{ON}}] = 0.01131$ for the standard case of FAMOUS_B calibrated parameters. Therefore the collapse is $\exp[0.00266/\epsilon]$ times more likely than its recovery, which is a factor 1.645 ± 0.115 for our value of $\epsilon = 0.0055 \pm 0.0008$.

A similar analysis can be done for the AMOC collapse under various freshwater flux parameters as a way to quantify the effect of different forcing strategies. In Smith and Gregory (2009) it is shown that the AMOC response is sensitive to the choice of hosing regions. By varying the fraction of freshwater forcing in different surface boxes, we can express this sensitivity in terms of relative likelihoods. Previously we used the noise parameters from the FAMOUS_B calibration, but now we vary these and compute for each different set of (A_N, A_T, A_S, A_{IP}) the most likely noise-induced collapse and associated noise. These parameters are changed using

$$(A_N, A_T, A_S, A_{IP}) = (\gamma_1, 1 - \gamma_1, -\gamma_2, \gamma_2 - 1)$$

with varying $0 \leq \gamma_1, \gamma_2 \leq 1$. Next, the noise vector σ is computed as

$$\sigma_i = f_{\text{norm}} \frac{A_i}{V_i}$$

with normalization factor

$$f_{\text{norm}} = 0.1063181 / \sqrt{\sum_i \left(\frac{A_i}{V_i}\right)^2}$$

such that the norm $\|\sigma\|$ is 0.1063181 as is the case for the original parameters, and a fair comparison can be made. Following these computations, the earlier used $(A_N, A_T, A_S, A_{IP}) = (0.070, 0.752, -0.257, -0.565)$ is achieved using $(\gamma_1, \gamma_2) = (0.09, 0.31)$. The results are in Table 1, where the ratio of the probability of an AMOC collapse for various (γ_1, γ_2) values compared to the probability of an AMOC collapse under the standard parameters are listed.

From Table 1 it follows that to increase the likelihood of an AMOC collapse the freshwater forcing needs to be redistributed with a higher fraction of fresh water into the northern box (increased γ_1) and a lower fraction of compensation into the southern box (decreased γ_2). However, these changes should not be overdone, as dumping all fresh water into the northern box, or compensating for it fully from the southern box would actually reduce the likelihood.

To examine the physical reasons behind the changes in likelihood, the scenario with the highest likelihood of col-

		γ_2				
		0	0.25	0.5	0.75	1
γ_1	0	0.71 ± 0.04	0.73 ± 0.04	0.62 ± 0.04	0.44 ± 0.05	0.27 ± 0.05
	0.25	1.41 ± 0.07	1.45 ± 0.08	1.30 ± 0.05	1.03 ± 0.01	0.72 ± 0.03
	0.5	1.10 ± 0.02	1.13 ± 0.02	1.06 ± 0.01	0.91 ± 0.02	0.72 ± 0.04
	0.75	0.64 ± 0.05	0.66 ± 0.04	0.65 ± 0.04	0.58 ± 0.05	0.51 ± 0.05
	1	0.37 ± 0.05	0.38 ± 0.06	0.37 ± 0.05	0.37 ± 0.06	0.33 ± 0.05

TABLE 1: The ratio of probabilities of an AMOC collapse under various hosing parameters (γ_1, γ_2) compared to the collapse under standard FAMOUS_B calibrated hosing parameters for $\epsilon = 0.0055 \pm 0.0008$. The fractions of the hosing are $(A_N, A_T, A_S, A_{IP}) = (\gamma_1, 1 - \gamma_1, -\gamma_2, \gamma_2 - 1)$, so increasing γ_1 results in more freshwater hosing in the N box and less into the T box, and increasing γ_2 results in more salinity compensation in the S box and less into the IP box. The bold values indicate an increased likelihood of an AMOC collapse.

lapse $((\gamma_1, \gamma_2) = (0.25, 0.25))$, and scenarios with either one of the parameters changed are analyzed. Their instantons are shown in the Fig. 5. Varying γ_1 yields the instantons in the left panels of Fig. 5. The differences in the salinities S_S and S_{IP} between scenarios are marginal ($O(10^{-2})$). As γ_1 increases a higher fraction of the freshwater is dumped into box N , and so the AMOC q shuts down more rapidly. The surplus salinity left behind in T cannot leave via box N and is then redistributed via gyres to S and IP and so the salinities here are slightly higher during the collapse. Moreover for lower γ_1 the T box is fresher, since with higher A_T more freshwater is simply deposited here. Similarly, as γ_1 increases the salinity S_N drops more rapidly as a greater amount of freshwater is put here.

As γ_1 is higher than the optimal value $\gamma_1 = 0.25$ the initial salinification becomes larger, while the subsequent freshwater pulse is sharper and higher. As discussed before the initial salinification puts the system into a transient state with a fresher T box, which destabilizes the AMOC, see also derivation (14). As γ_1 increases, it becomes harder to directly freshen T , and so the higher initial salinification with a temporary stronger AMOC is required. However, S_T is still higher than usual, so the upcoming freshwater pulse also needs to be stronger. On the other hand, if γ_1 decreases from the optimal value the only way to get the necessary fresh water into box N is via advection and gyre transport, which is ineffective as the freshwater input into T also leaks to the S and IP boxes. So some freshwater input directly into N helps, especially since V_N is relatively small so its salinity is more easily changed. Concluding, for γ_1 there is an optimal compromise: γ_1 needs to be low enough to directly freshen the stabilizing saline thermocline, yet high enough to add freshwater to the relatively small N box.

In the right panels of Fig. 5 again the optimal hosing scenario is taken, but now γ_2 is varied. Compared to varying γ_1 the salinity and likelihood changes across hosing scenarios are quite small. The salinity changes in the di-

rectly affected boxes S and IP are only of order $O(10^{-2})$. The effects are straightforward: an increased γ_2 implies a higher fraction of salinification into box IP and so S_{IP} rises while S_S drops. For the boxes N and T there are hardly any differences. Also the optimal freshwater perturbations change only marginally.

The changes in likelihood can be derived from the graphs in Fig. 5. As γ_2 is put to zero ($A_S = 0$) there is no way to directly control S_S and so any required marginal changes are done via ineffective gyre and AMOC transport. So the likelihood slightly decreases. On the other hand, decreasing A_{IP} has a significant negative effect on the likelihood of collapse. This can be understood with the zoomed inset in the S_T -graph (Fig. 5g). As A_{IP} decreases the southern box becomes more saline, while the Indo-Pacific freshens. The transport from S to T is larger than the one from IP to T , since $K_N + \gamma q \approx 11$ Sv while $(1 - \gamma)q \approx 9$ Sv (taking $q \approx 15$ Sv). So a saltier Southern Ocean means a saltier Atlantic thermocline which stabilizes the AMOC (see (14)) and hence decreases the likelihood of collapse.

b. Linear Deterministic versus Optimal Stochastic Forcing

In this section, the behaviour of the AMOC in the noise-induced transition following the instanton is compared to its deterministic behaviour in a bifurcation-induced tipping. For the latter, we force the AMOC with a prescribed freshwater flux which is piecewise linear time dependent similar to the method of Wood et al. (2019). The goal there was to force the AMOC to stay close to equilibrium and hence the bifurcation tipping was produced. In Fig. 6b, the graph from Wood et al. (2019) is qualitatively reproduced with the following deterministic hosing procedure:

$$\dot{\phi}(t) = f(\phi(t)) + \sigma h(t)$$

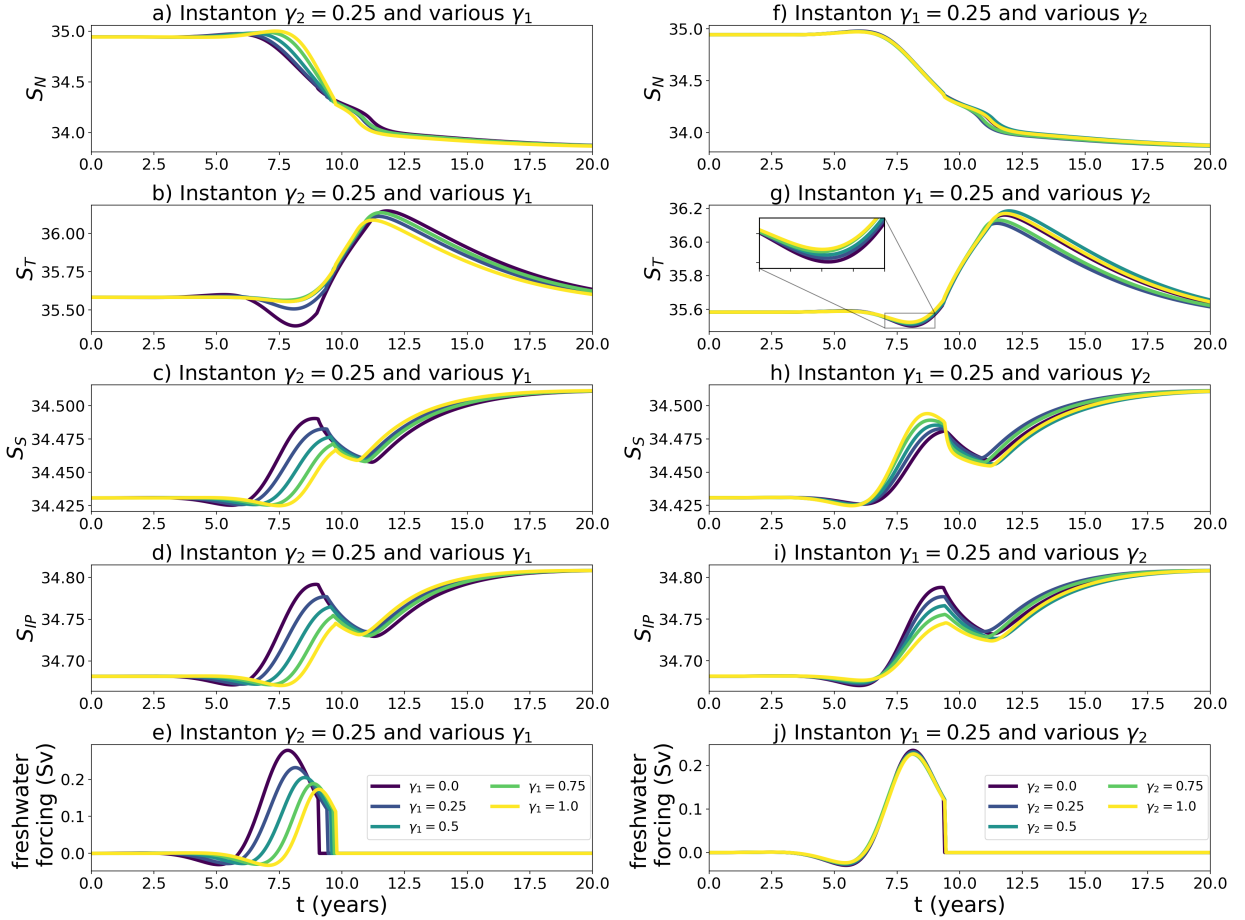


FIG. 5: The instantons for varying γ_1 (left) and varying γ_2 (right) with dimensional salinities S_N (a, f), S_T (b, g), S_S (c, h) and S_{IP} (d, i) and the associated optimal freshwater forcings (e, j).

where

$$h(t) = \begin{cases} -0.012t & \text{for } t < 25 \\ -0.3 + 0.012(t - 25) & \text{for } t > 25. \end{cases} \quad (18)$$

where σ follows from the original hosing parameters from the FAMOUS_B calibration. Note that with this simple hosing procedure, the amount of hosing sufficient for a transition is not minimized nor the stable OFF-state was reached. Moreover, the graph in the original paper was produced with the FAMOUS_A hosing parameters. In Fig. 6a the instanton is shown, directly followed by the ‘anti’-instanton, so it is the most likely transition path from ON to OFF and back. Both are computed for the original hosing fractions and already discussed in section 4. The comparison of the two graphs in Fig. 6 illuminates the different behaviors of a noise-induced and a bifurcation-induced tipping.

Firstly, the salinity S_T is in the deterministic hosing simulation much lower than for the instanton trajectory. In the former fresh water is continuously put into the thermocline box causing its salinity to stay low. But along the instanton one sees S_T bouncing back, since an AMOC collapse means that salt is no longer transported northward out of the thermocline. Secondly, the salinity S_N drops less rapidly than in the instanton’s case. The main reason is that in the latter case a sharp fresh water pulse is introduced to the T box, which rapidly freshens the northern box via the AMOC before it collapses, whereas in the former case the fresh water is introduced gradually so S_N drops less rapidly. Thirdly, smaller features are seen in the trajectories of S_{IP} and S_S . For these boxes the salinities grow more slowly since fresh water is extracted more gently. It seems that due to the excess fresh water extraction in the hosing the salinities of these two boxes and of the B box is artificially higher. Lastly, the recovery of the AMOC shows the same overshooting for both freshwater

forcing strategies: in both cases we need $S_T \approx 36.58$, since this is just salty enough to reactivate the AMOC. After this, all the salt is suddenly transported northward, causing the huge rise and drop in S_N and S_T respectively. Small salinity differences after the recovery between the hosing strategies are because in the linear hosing case fresh water is still being extracted from T , and so additional salt is transported northward causing a higher S_N . That the bifurcation and noise-induced tipping do not differ that much when the AMOC recovers, could also be concluded from figures 4e, f and g, as the system stays close to the shifting stable root.

Comparing the bifurcation points of the system with the computed optimal forcings also indicate the similarity between the most likely noise-induced and bifurcation-induced recovery. The AMOC has two stable states for $h \in (-0.069, 0.025)$, i.e. $(-0.066, 0.180)$ Sv of freshwater input into N and T . So in the quasi-equilibrium approach done in Fig. 6b the AMOC is in a mono-stable OFF-regime and ON-regime for $t \in (6, 44)$ years and $t > 52$ years respectively. The optimal forcing for the noise-induced AMOC collapse only crosses the bifurcation point briefly for 1.7 years ($t \in (12, 13.7)$ years, see Fig. 2c) and this ends already 1.3 years before reaching the separatrix. A brief time interval where no unstable ON-state exists (see Fig. 4b) is enough to put the AMOC in an unstable regime from whereon it collapses even though a stable ON-state exists again (see Fig. 4c). Contrarily, the optimal forcing for the recovery crosses the bifurcation threshold for $t \in (15.9, 25)$ years continuing till the separatrix, see Fig. 2d. So here the separatrix is crossed when no stable OFF-state exists, similar to a bifurcation-induced tipping. This can also be deduced from Fig. 4e, f and g: the crossing happens when eventually there is no stable root for $q < 0$ i.e. the OFF-regime no longer sees any state with a decreasing q for the given salinity ϕ_2 . Hence, the most likely noise-induced collapse only crosses the bifurcation briefly and before reaching the separatrix, while the noise-induced collapse has a sustained forcing that crosses this bifurcation threshold through to the separatrix and behaves like a bifurcation-induced tipping.

6. Summary and Discussion

In this work we computed the most likely paths of an AMOC collapse and recovery in a stochastic version of the Wood et al. (2019) model. This is a conceptual box-model representation of the World Ocean which is calibrated to the AOGCM FAMOUS. We added the stochasticity to allow for noise-induced tipping of the AMOC, which was justified as a representation of the $P - E$ annual variation in the North Atlantic. Thanks to the model's simplicity the instantons can be readily computed. Using this method we made a thorough analysis of noise-induced transitions of the AMOC. The most likely collapse of the AMOC will be

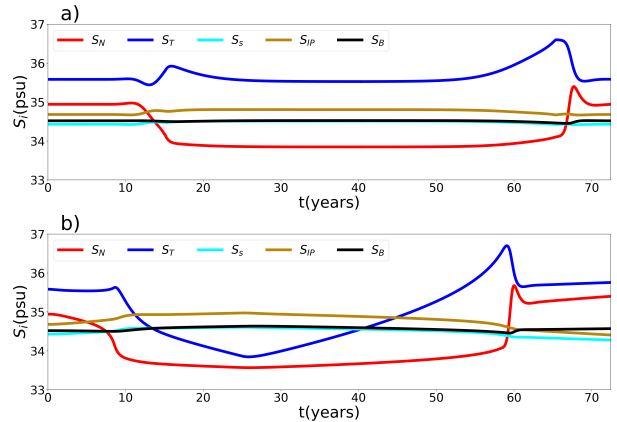


FIG. 6: (Top, a) The instanton directly followed by the ‘anti’-instanton, and (Bottom, b) the deterministic model behaviour under the prescribed freshwater forcing (18) for dimensional salinities S_N (red), S_T (blue), S_S (cyan), S_{IP} (brown) and S_B (black).

preempted by an initial strengthening of the AMOC, which puts it into a less stable transient state. This is followed by a sharp freshwater pulse into the Atlantic thermocline such that the AMOC ends up in an unstable regime from whereon it collapses due to its own deterministic dynamics. Contrarily, the noise-induced recovery is quite close to the shifting equilibrium and is comparable to a bifurcation tipping.

By comparing the actions of the instantons the ratios of their probabilities in the low-noise limit were computed. Any biases towards an ON or OFF-state due to the hosing method are now eliminated, accommodating a quantitative analysis of various hosing methods. This is a strength of the method since probabilities are determined and not merely mechanisms or theoretical possibilities of the hosing methods. This showed that to maximize the probability of an AMOC collapse most of the freshwater forcing needs to be added to the Atlantic thermocline, such that it cannot salinify the northern Atlantic, while only a small fraction of the compensation needs to be in the Southern Ocean since from here the Atlantic thermocline can most easily be salinified.

The limitations of our approach are firstly the assumptions on the freshwater noise. Adding a white noise process for freshwater forcing to the model has been done many times (Cessi 1994; Timmermann and Lohmann 2000; Castellana et al. 2019) and simplifies many computations, but under climate change this noise can be coloured and state-dependent. Furthermore, the system needs to be in the limit of low noise. This is the case for the model used here, and arguably holds for other AMOC models, as the noise compared to the AMOC strength should not depend too much on the model choice. The computation itself of

the instanton can be tedious for more detailed ocean models and was here limited to low-dimensional continuous models. However, formally the Freidlin-Wentzell action holds for infinite dimensional stochastic PDE's (SPDEs), and can be extended to multiplicative and even non-Gaussian noise (Grafke and Vanden-Eijnden 2019).

Lastly, this study's relevance relies on the present-day AMOC being in a multi-stable regime in order for noise-induced transitions to be possible. As mentioned it is debatable whether the observed negative AMOC induced freshwater transport at the southern boundary of the Atlantic basin is an indicator of this multi-stability. We think that the evidence in favour of this claim is strong enough that the possibility of multi-stability should not be ignored. A range of studies have shown this indicator to be reliable in a hierarchy of ocean models (de Vries and Weber 2005; Dijkstra 2007; Huisman et al. 2010) and even in a state-of-the-art global climate model (van Westen and Dijkstra 2023). However, there are also numerous studies arguing the present-day AMOC to be mono-stable (Jackson 2013; Jackson et al. 2022). That said, we should consider that this indicator in these models is sensitive to model biases (Mecking et al. 2017). This debate is far from settled and outside the study's scope.

It will obviously be a challenge to compute instantons in spatially extended models of the AMOC that are governed by SPDEs, which would provide the identification of the most vulnerable freshwater forcing regions to tip the AMOC. From this, likely ensemble simulations can be designed to optimize the probability of a noise induced AMOC transition, which can possibly be used in global climate models. Also –given a computed probability of an AMOC collapse (Castellana et al. 2019)– the probabilities for other forcing scenarios in the low-noise limit can be computed. Lastly, as instantons have been used as precursors for noise-induced tipping in more simplified models (Giorgini et al. 2020), it is worth exploring whether they can be used to identify early warning signals of an approaching AMOC collapse.

APPENDIX A

Numerical solution of the instanton equations

We want to solve the Hamiltonian equations (6) with boundary conditions $\phi(0) = x$ and $\phi(T) = y$. Reformulating it as a minimization problem of the cost function yields:

$$\begin{aligned} J(\phi(t), \theta(t), \mu(t)) &= \frac{1}{2} \int_0^T \langle \theta(t), a\theta(t) \rangle dt \\ &+ \int_0^T \langle \mu(t), \dot{\phi}(t) - f(\phi(t)) - a\theta(t) \rangle dt \\ &+ \langle \beta, \phi(T) - y \rangle + \lambda \|\phi(T) - y\|^2 \end{aligned}$$

where $\mu : [0, T] \rightarrow \mathbb{R}^d$ and $\beta \in \mathbb{R}^d$ are Lagrange multipliers to fulfill the constraints and λ is an additional penalty term. Equalizing the variational derivatives to zero:

$$\begin{aligned} \frac{\delta J}{\delta \theta} = 0 &\iff a(\theta(t) - \mu(t)) = 0 \\ \frac{\delta J}{\delta \phi} = 0 &\iff -\dot{\mu}(t) - (\nabla f(\phi(t)))^T \mu(t) = 0 \\ \frac{\delta J}{\delta \mu} = 0 &\iff \dot{\phi}(t) - f(\phi(t)) - a\theta(t) = 0 \end{aligned}$$

and for the constraints:

$$\begin{aligned} \frac{\partial J}{\partial \lambda} &= \|\phi(T) - y\|^2 = 0 \\ \nabla_{\beta} J &= \phi(T) - y = 0. \end{aligned}$$

Minimizing this cost function together with initial condition $\phi(0) = x$ solves the instanton equations. This pseudo-code is used to find the minimum:

Given initial $\phi^0(t), \theta^0(t), \mu^0(t)$

Repeat:

Repeat until $\|\phi^k(t) - \mu^{k+1}(t)\| < \text{tol}$:

Integrate forward

$$\dot{\phi}^{k+1}(t) = f(\phi^k(t)) + a\theta^k(t)$$

with $\phi^{k+1}(0) = x$

Integrate backward

$$\dot{\mu}^{k+1}(t) = -\nabla f(\phi^{k+1}(t))^T \mu^k(t)$$

with $\mu^{k+1}(T) = -(2\lambda(\phi^{k+1}(T) - y) + \beta)$

$$\theta^{k+1}(t) = \theta^k - \alpha(\theta^k(t) - \mu^{k+1}(t))$$

with $\alpha = \max \{ \alpha | J(\phi^{k+1}, \theta^{k+1}(t), \mu^{k+1}) < J(\phi^{k+1}, \theta^k, \mu^{k+1}) \}$

$$\beta \rightarrow \beta + \lambda(\phi^{k+1}(T) - y)$$

$$\lambda \rightarrow f_{\lambda} \lambda$$

where $f_{\lambda} > 1$ a factor to update λ . The algorithm searches for the end condition $\theta(T) = -\beta$ such that $\phi(T) = y$. The equation for the path $\phi(t)$ is integrated forward in time, while that for the conjugate momentum is integrated backward in time to ensure numerical stability. To speed up convergence we added $\theta = 0$ after q switches sign. This is justified as the model converges deterministically to the new stationary point after this switch following the analysis done in section 4b.

APPENDIX B

Used Parameter Values

In Table B1 the parameter values of the non-dimensional model are provided. The volumes and transports are written in units 10^6m^3 and Sv respectively, such that most parameters have an order of magnitude $\mathcal{O}(10^{-2}) - \mathcal{O}(10^2)$. The parameters that do not fulfill this always occur in reasonable ratios: $t_d/V_0 \sim 0.31536 \cdot 10^{-6} \text{m}^{-3}\text{s}$ and $C/(S_0V_0) \sim 127$.

APPENDIX C

Relative Likelihood in Low-Noise Limit

Consider two stochastic systems as in (1) with the same smallness-parameter ϵ indicating the noise amplitude:

$$\begin{aligned} dX_t^1 &= f_1(X_t^1) dt + \sigma_1 \sqrt{\epsilon} dW_t^1 \\ dX_t^2 &= f_2(X_t^2) dt + \sigma_2 \sqrt{\epsilon} dW_t^2 \end{aligned}$$

with $X_t^i \in \mathbb{R}^d$ the state vector, $f_i : \mathbb{R}^d \rightarrow \mathbb{R}^d$ the deterministic drift, W_t^i a k -dimensional Wiener process, and $\sigma_i \in \mathbb{R}^{d \times k}$ distributing the noise for $i \in \{1, 2\}$. We need $\|\sigma_1\| = \|\sigma_2\|$ in order for the noise amplitudes to be the same in both systems. Again we state equation (2) for both systems:

$$\epsilon \log \left(\mathbb{P} \left[\sup_{t \in [0, T]} \|X_t^i - \phi^i(t)\| < \delta \right] \right) = -S_T^i[\phi^i] + \mathcal{O}(\epsilon)$$

where S_T^i is the Freidlin-Wentzell action for system i and $\phi^i(t) : [0, T] \rightarrow \mathbb{R}^d$ is a path in that system. The relative likelihood in the low-noise limit between path $\phi^1(t)$ in the first and $\phi^2(t)$ in the second system is now computed as

$$\epsilon \log \left(\frac{\mathbb{P} \left[\sup_{t \in [0, T]} \|X_t^1 - \phi^1(t)\| < \delta \right]}{\mathbb{P} \left[\sup_{t \in [0, T]} \|X_t^2 - \phi^2(t)\| < \delta \right]} \right) = S_T^2[\phi^2] - S_T^1[\phi^1] + \mathcal{O}(\epsilon)$$

and hence

$$\frac{\mathbb{P} \left[\sup_{t \in [0, T]} \|X_t^1 - \phi^1(t)\| < \delta \right]}{\mathbb{P} \left[\sup_{t \in [0, T]} \|X_t^2 - \phi^2(t)\| < \delta \right]} \asymp \exp \left[(S_T^2[\phi^2] - S_T^1[\phi^1]) / \epsilon \right].$$

Acknowledgments. We would like to thank Reyk Börner, Raphael Römer, Jason Frank and the two anonymous reviewers for their insightful suggestions. J.S. and H.A.D. are funded by the European Research Council through ERC-AdG project TAOC (project 101055096). T.G. acknowledges support from EPSRC projects EP/T011866/1 and EP/V013319/1. For the purpose of open access, the authors have applied a Creative Commons Attribution (CC BY) licence to any Author Accepted Manuscript version arising from this submission.

Data availability statement. The results can be readily reproduced using the described method and the stated parameter values.

References

- Alkhayoun, H., P. Ashwin, L. C. Jackson, C. Quinn, and R. A. Wood, 2019: Basin bifurcations, oscillatory instability and rate-induced thresholds for atlantic meridional overturning circulation in a global oceanic box model. *Proceedings of the Royal Society A*, **475** (2225), 20190051.
- Blyuss, K., and Y. Kyrychko, 2023: Sex, ducks, and rock “n” roll: Mathematical model of sexual response. *Chaos: An Interdisciplinary Journal of Nonlinear Science*, **33** (4).
- Boers, N., 2021: Observation-based early-warning signals for a collapse of the Atlantic Meridional Overturning Circulation. *Nature Climate Change*, **11** (8), 680–688, <https://doi.org/10.1038/s41558-021-01097-4>.
- Börner, R., R. Deeley, R. Römer, T. Grafke, V. Lucarini, and U. Feudel, 2023: Saddle avoidance of noise-induced transitions in multiscale systems. *arXiv preprint arXiv:2311.10231*.
- Caesar, L., S. Rahmstorf, A. Robinson, G. Feulner, and V. Saba, 2018: Observed fingerprint of a weakening Atlantic Ocean overturning circulation. *Nature*, **556** (7700), 191–196, <https://doi.org/10.1038/s41586-018-0006-5>, URL <http://www.nature.com/articles/s41586-018-0006-5>.
- Castellana, D., S. Baars, F. W. Wubs, and H. A. Dijkstra, 2019: Transition probabilities of noise-induced transitions of the atlantic ocean circulation. *Scientific Reports*, **9** (1), 20284.
- Cessi, P., 1994: A simple box model of stochastically forced thermohaline flow. *Journal of Physical Oceanography*, **24** (9), 1911–1920.
- Cimatoribus, A. A., S. S. Drijfhout, and H. A. Dijkstra, 2014: Meridional overturning circulation: Stability and ocean feedbacks in a box model. *Climate dynamics*, **42**, 311–328.
- de Vries, P., and S. L. Weber, 2005: The atlantic freshwater budget as a diagnostic for the existence of a stable shut down of the meridional overturning circulation. *Geophysical Research Letters*, **32** (9).
- Dee, D. P., and Coauthors, 2011: The era-interim reanalysis: Configuration and performance of the data assimilation system. *Quarterly Journal of the royal meteorological society*, **137** (656), 553–597.
- Dijkstra, H. A., 2007: Characterization of the multiple equilibria regime in a global ocean model. *Tellus A: Dynamic Meteorology and Oceanography*, **59** (5), 695–705.
- Ditlevsen, P., and S. Ditlevsen, 2023: Warning of a forthcoming collapse of the Atlantic meridional overturning circulation. *Nature Communications*, **14** (1), 4254.
- Ditlevsen, P. D., and S. J. Johnsen, 2010: Tipping points: Early warning and wishful thinking. *Geophysical Research Letters*, **37** (19).
- Frajka-Williams, E., and Coauthors, 2019: Atlantic meridional overturning circulation: Observed transport and variability. *Frontiers in Marine Science*, 260.
- Freidlin, M. I., and A. D. Wentzell, 1998: *Random perturbations*. Springer.

Parameter Values		
V_0 (10^6m^3)	10^{10}	volume scaling parameter
V_1	3.261	volume northern box
V_2	7.777	volume Atlantic thermocline box
V_3	8.897	volume southern box
V_4	22.02	volume Indo-Pacific box
V_5	86.49	volume bottom box
t_d (s)	$3.1536 \cdot 10^9$	time scaling parameter
S_0 (psu)	35	salinity scaling parameter
C ($10^6\text{m}^3\text{psu}$)	$4.446304026 \cdot 10^{13}$	total salinity in basin
α ($\text{kg}/\text{m}^3\text{K}$)	0.12	thermal coefficient
β (kg/m^3)	0.79	saline coefficient
γ	0.39	proportion Cold Water Path
η (Sv)	74.492	S-B box mixing parameter
K_N (Sv)	5.456	northern subtropical gyre coefficient
K_S (Sv)	5.447	southern subtropical gyre coefficient
K_{IP} (Sv)	96.817	Indo-Pacific gyre coefficient
F_N (Sv)	0.384	northern freshwater flux
F_T (Sv)	-0.723	Atlantic thermocline freshwater flux
F_S (Sv)	1.078	southern freshwater flux
F_{IP} (Sv)	-0.739	Indo-Pacific freshwater flux
T_S (K)	4.773	southern box temperature
T_0 (K)	2.65	base temperature
μ ($10^{-6}\text{m}^{-3}\text{sK}$)	0.055	heat transport coefficient
λ ($10^6\text{m}^6/\text{kg s}$)	27.9	MOC-density difference coefficient

TABLE B1: Used Parameter Values

- Giorgini, L. T., S. H. Lim, W. Moon, and J. S. Wettlaufer, 2020: Precursors to rare events in stochastic resonance. *Europhysics letters*, **129** (4), 40 003.
- Grafke, T., R. Grauer, and T. Schäfer, 2015: The instanton method and its numerical implementation in fluid mechanics. *Journal of Physics A: Mathematical and Theoretical*, **48** (33), 333 001.
- Grafke, T., and E. Vanden-Eijnden, 2019: Numerical computation of rare events via large deviation theory. *Chaos: An Interdisciplinary Journal of Nonlinear Science*, **29** (6).
- Hawkins, E., R. S. Smith, L. C. Allison, J. M. Gregory, T. J. Woollings, H. Pohlmann, and B. De Cuevas, 2011: Bistability of the atlantic overturning circulation in a global climate model and links to ocean freshwater transport. *Geophysical Research Letters*, **38** (10).
- Hestenes, M. R., 1969: Multiplier and gradient methods. *Journal of optimization theory and applications*, **4** (5), 303–320.
- Hofmann, M., and S. Rahmstorf, 2009: On the stability of the atlantic meridional overturning circulation. *Proceedings of the National Academy of Sciences*, **106** (49), 20 584–20 589.
- Huisman, S. E., M. Den Toom, H. A. Dijkstra, and S. Drijfhout, 2010: An indicator of the multiple equilibria regime of the atlantic meridional overturning circulation. *Journal of Physical Oceanography*, **40** (3), 551–567.
- Jackson, L., 2013: Shutdown and recovery of the amoc in a coupled global climate model: The role of the advective feedback. *Geophysical Research Letters*, **40** (6), 1182–1188.
- Jackson, L., and R. Wood, 2018: Hysteresis and resilience of the amoc in an eddy-permitting gcm. *Geophysical Research Letters*, **45** (16), 8547–8556.
- Jackson, L. C., and Coauthors, 2022: Understanding amoc stability: the north atlantic hosing model intercomparison project. *Geoscientific Model Development Discussions*, **2022**, 1–32.
- Jacques-Dumas, V., R. M. van Westen, and H. A. Dijkstra, 2024: Estimation of amoc transition probabilities using a machine learning based rare-event algorithm. *arXiv preprint arXiv:2401.10800*.
- Lenton, T., and Coauthors, 2007: Effects of atmospheric dynamics and ocean resolution on bi-stability of the thermohaline circulation examined using the grid enabled integrated earth system modelling (genie) framework. *Climate Dynamics*, **29**, 591–613.
- Lenton, T. M., H. Held, E. Kriegler, J. W. Hall, W. Lucht, S. Rahmstorf, and H. J. Schellnhuber, 2008: Tipping elements in the earth’s climate system. *Proceedings of the national Academy of Sciences*, **105** (6), 1786–1793.
- Lucarini, V., and P. H. Stone, 2005: Thermohaline circulation stability: A box model study. part i: Uncoupled model. *Journal of climate*, **18** (4), 501–513.
- Marotzke, J., 2000: Abrupt climate change and thermohaline circulation: Mechanisms and Predictability. *Proc. Natl. Acad. Sci.*, **97**, 1347–1350.
- Mecking, J., S. Drijfhout, L. Jackson, and M. Andrews, 2017: The effect of model bias on atlantic freshwater transport and implications for

- amoc bi-stability. *Tellus A: Dynamic Meteorology and Oceanography*, **69** (1), 1299–1310.
- Mikosch, T., 1998: *Elementary stochastic calculus with finance in view*. World scientific.
- Nocedal, J., and S. J. Wright, 1999: *Numerical optimization*. Springer.
- Puhalskii, A., 2004: On some degenerate large deviation problems.
- Rahmstorf, S., 1996: On the freshwater forcing and transport of the atlantic thermohaline circulation. *Climate Dynamics*, **12**, 799–811.
- Rahmstorf, S., and Coauthors, 2005: Thermohaline circulation hysteresis: A model intercomparison. *Geophysical Research Letters*, **32** (23).
- Romanou, A., and Coauthors, 2023: Stochastic bifurcation of the north atlantic circulation under a midrange future climate scenario with the nasa-giss modele. *Journal of Climate*, **36** (18), 6141–6161.
- Rooth, C., 1982: Hydrology and ocean circulation. *Progress in Oceanography*, **11** (2), 131–149.
- Schorlepp, T., T. Grafke, S. May, and R. Grauer, 2022: Spontaneous symmetry breaking for extreme vorticity and strain in the three-dimensional navier–stokes equations. *Philosophical Transactions of the Royal Society A*, **380** (2226), 20210051.
- Smith, R., 2012: The famous climate model (versions xfxwb and xfhcc): description update to version xdbua. *Geoscientific Model Development*, **5** (1), 269–276.
- Smith, R. S., and J. M. Gregory, 2009: A study of the sensitivity of ocean overturning circulation and climate to freshwater input in different regions of the north atlantic. *Geophysical research letters*, **36** (15).
- Smith, R. S., J. M. Gregory, and A. Osprey, 2008: A description of the famous (version xdbua) climate model and control run. *Geoscientific Model Development*, **1** (1), 53–68.
- Srokosz, M. A., N. P. Holliday, and H. L. Bryden, 2023: Atlantic overturning: new observations and challenges. The Royal Society, 20220196 pp.
- Stommel, H., 1961: Thermohaline convection with two stable regimes of flow. *Tellus*, **13** (2), 224–230.
- Taylor, J. R., 2005: *Classical mechanics*, Vol. 1. Springer.
- Timmermann, A., and G. Lohmann, 2000: Noise-induced transitions in a simplified model of the thermohaline circulation. *Journal of Physical Oceanography*, **30** (8), 1891–1900.
- van Westen, R. M., and H. A. Dijkstra, 2023: Asymmetry of amoc hysteresis in a state-of-the-art global climate model. *Geophysical Research Letters*, **50** (22), e2023GL106088.
- Weijer, W., and Coauthors, 2019: Stability of the Atlantic Meridional Overturning Circulation: A Review and Synthesis. *Journal Of Geophysical Research-Oceans*, **124** (8), 5336 – 5375, <https://doi.org/10.1029/2019jc015083>.
- Woillez, E., and F. Bouchet, 2020: Instantons for the destabilization of the inner solar system. *Physical Review Letters*, **125** (2), 021101.
- Wood, R. A., J. M. Rodríguez, R. S. Smith, L. C. Jackson, and E. Hawkins, 2019: Observable, low-order dynamical controls on thresholds of the atlantic meridional overturning circulation. *Climate Dynamics*, **53**, 6815–6834.